White Rose Research Online
eprints@whiterose.ac.uk
https://eprints.whiterose.ac.uk
Universities of Leeds, Sheffield and York

Deposited via The University of Sheffield.

White Rose Research Online URL for this paper:
https://eprints.whiterose.ac.uk/id/eprint/238862/

Version: Accepted Version

Article:

Zhao, H., Liu, Z., Gao, J. et al. (2026) Crystallographic and morphological characteristics of acicular ferrite and their formation mechanisms in HSLA steels. Journal of Materials Science & Technology, 271. pp. 247-258. ISSN: 1005-0302

https://doi.org/10.1016/j.jmst.2026.02.010

© 2026 The Authors. Except as otherwise noted, this author-accepted version of a journal article published in Journal of Materials Science & Technology is made available via the University of Sheffield Research Publications and Copyright Policy under the terms of the Creative Commons Attribution 4.0 International License (CC-BY 4.0), which permits unrestricted use, distribution and reproduction in any medium, provided the original work is properly cited. To view a copy of this licence, visit http://creativecommons.org/licenses/by/4.0/

Reuse
This article is distributed under the terms of the Creative Commons Attribution (CC BY) licence. This licence allows you to distribute, remix, tweak, and build upon the work, even commercially, as long as you credit the authors for the original work. More information and the full terms of the licence here: https://creativecommons.org/licenses/

Takedown
If you consider content in White Rose Research Online to be in breach of UK law, please notify us by emailing eprints@whiterose.ac.uk including the URL of the record and the reason for the withdrawal request.

UNIVERSITY OF LEEDS
University of Sheffield
UNIVERSITY of York

Crystallographic and morphological characteristics of acicular ferrite and their formation mechanisms in HSLA steels

Haitao Zhao[a,e], Zanyang Liu [a], Junheng Gao[a,e,*], Honghui Wu[a,e], Zhongzhu Liu[c,*],
Guodong Zhang[c], Chaolei Zhang[a,e], Yuhe Huang[a,e], Jun Lu[a,e], Shuize Wang[a,e,*],
Bradley P. Wynne[d], Xinping Mao[a,e], Eric J. Palmiere[b,*]

[a] Institute for Carbon Neutrality, University of Science and Technology Beijing, Beijing 100083, China

[b] The University of Sheffield, School of Chemical, Materials and Biological Engineering, Sir Robert Hadfield Building, Mappin Street, Sheffield S1 3JD, United Kingdom

[c] Department of Niobium Products, CITIC Metal Co., Ltd., Beijing 100027, China

[d] Department of Mechanical and Aerospace Engineering, University of Strathclyde, 75 Montrose Street, Glasgow G1 1XJ, United Kingdom

[e] Institute for Steel Sustainable Technology, Liaoning Academy of Materials, Shenyang 110004, China

*Corresponding authors E-mail: e.j.palmiere@sheffield.ac.uk; junhenggao@ustb.edu.cn; Liuzz3@citic.com; wangshuize@ustb.edu.cn

Abstract:

The crystallographic and morphological characteristics of acicular ferrite (AF) and their formation mechanisms were investigated in this research. A high-strength low-alloy steel was processed to promote AF formation, and a numerical fitting method was employed to reconstruct the deformed austenite orientations. Comprehensive crystallographic analysis revealed that the crystallographic characteristics of AF are manifested in the selection of variants from multiple close-packed plane (CP) and Bain groups and the near random variant pairing. This is distinct from those observed in other bainitic microstructures in the literature exhibiting variants selected from either the same CP or the same Bain group and the preferential variant pairing. These unique crystallographic features arise from multi-variant intragranular nucleation, arrest of lengthening laths and self-accommodation of the transformation shape strain, driven by austenite deformation and proper cooling. Correlative morphology characterization and three-dimensional atom probe results indicate that the boundaries between AF laths become metallographically distinguishable through crystal faceting, martensite/austenite constituent delineating, and surface protrusions induced by carbon segregation at grain boundaries. The morphological features of AF—chaotic grain arrangements and irregular grain shapes—are direct consequences of AF’s distinct crystallographic characteristics and the above boundary revelation mechanisms. These findings advance the understanding and characterization of AF and provide insight into weakening variant selection and forming random variant pairing by austenite deformation and appropriate cooling.

Keywords: Acicular Ferrite; Orientation Relationship; Variant Selection; Variant Pairing; Morphological Characteristics.

1 Introduction

Acicular ferrite (AF) is a microstructure emerged alongside the thermomechanical controlled processing and accelerated cooling techniques for high-strength low-alloy (HSLA) steels [1]. It was firstly defined by Smith et al. [2] in 1972 as “a highly substructured, non-equiaxed ferrite that forms upon continuous cooling by a mixed diffusion and shear mode of transformation that begins at a temperature slightly higher than the upper bainite transformation range”. AF is known to possess an excellent combination of strength and toughness, making it a key target microstructure in the design of HSLA steels [3].

Despite the similar transformation mechanisms and strengths between AF and bainitic ferrite (BF), AF is usually separated from BF when describing microstructures [4–6]. This is mainly because AF grains are chaotically arranged and irregularly shaped [7], in contrast to the highly organised BF microstructures which contain packets of parallel laths [1]. Furthermore, the toughness of AF is considerably higher than that of BF, because of the higher density of high angle grain boundaries (HAGBs) in AF [8].

Extensive studies have been carried out on AF in HSLA steels, yet there are still some unclear aspects of AF, especially its crystallographic characteristics and the mechanism responsible for its unique crystallographic and morphological features. Crystallographic characteristics have profound influences on the morphology, grain boundary and mechanical properties of bainitic and martensitic microstructures [9–11]. For displacive transformations in steels, orientations of the transformation products and their parent grains are related by an orientation relationship (OR) [12]. Owing to this OR and the crystallography symmetry of austenite, up to 24 product orientations (i.e. variants) can be theoretically formed within a single austenite grain [13, 14]. Ideally, these variants should appear randomly. However, studies have shown that certain variants are preferentially selected [15–17], which is called variant selection. Moreover, those variants selected are not formed side by side randomly. Instead, certain pairs of variants are favoured [18, 19], which is called variant pairing.

Given that AF transformation mechanism is bainitic, crystallographic information including the OR, variant selection, variant pairing and the mechanism behind are essential for a complete characterisation and thorough understanding of AF in HSLA steels. Simultaneously, it has long been recognized that AF exhibits morphological characteristics distinctly different from those of BF, including irregular grain shape, chaotic and intersecting grain arrangement. However, the underlying mechanisms responsible for these morphological features have not been adequately explained.

Analysis for AF crystallographic characteristics still remains challenging. First, the volume fraction of retained austenite in HSLA steels after continuous cooling is very low, making it difficult to reliably determine its orientation using EBSD. Second, austenite deformation is a prerequisite for AF transformation because AF typically nucleates on deformation-induced substructures in austenite [20, 21]. The orientations of deformed austenite are even more difficult to resolve from EBSD data. Finally, since AF transformation typically occurs at relatively slow cooling rates or high temperatures [22, 23], reconstructive transformation products, e.g. polygonal ferrite (PF) and quasi-polygonal ferrite (QF), usually exist in the final microstructures and interfere with the crystallographic analysis of AF.

In this study, a commercial HSLA steel was subjected to plane strain compression followed by continuous cooling to obtain a microstructure containing AF. By encouraging coarse-grained austenite, the interference from reconstructive transformation products (PF and QF) was minimized. The numerical fitting method proposed by Miyamoto et al. [24] was adopted to reconstruct the local orientations of deformed parent austenite from the measured orientations of the transformation products. Crystallographic characteristics of AF—including the OR, variant selection and variant pairing—were systematically investigated, and the mechanisms responsible for the weakened variant selection and the nearly random variant pairing observed in

AF were clarified. Finally, how the morphology of AF becomes observable and the origins of the distinctive AF morphology were elucidated, through correlative morphology characterization and three-dimensional atom probe analysis.

2 Materials and methods

Plane strain compression tests were conducted on a commercially produced HSLA X80 pipeline steel having the chemical composition of Fe-0.045C-1.43Mn-0.14Si-0.09Nb-0.21Cr-0.12Ni-0.21Cu-0.01Ti (wt.%). To fully dissolve the niobium carbide precipitates and develop a large austenite grain size, specimens underwent austenitization at 1250 °C for 2 h in an argon atmosphere, followed by water quenching directly from 1250 °C to room temperature.

During testing, the heat-treated samples were reheated to 1200 °C at a rate of 10 °C/s, held for 2 min to achieve thermal equilibration, and then cooled at a rate of 5 °C/s to 950 °C for a strain of 0.5 at a constant true strain rate of 10 s^{-1}. After deformation, the samples were cooled from 950 °C to 500 °C at a rate of 10 °C/s, followed by slow cooling from 500 °C to 350 °C at a rate of 1 °C/s and finally water quenching from 350 °C to room temperature. Two additional samples were processed in the same manner, except that they were water quenched before and after the austenite deformation to examine the austenite microstructure. The schematic illustration of solid solution heat treatment and thermomechanical testing profile is shown in Fig. S1. The details of the plane strain compression tests are provided in the Supplementary materials [25, 26].

Samples for metallographic observations were sectioned on the rolling direction (RD) –normal direction (ND) plane and prepared. 2% nital was used to show the transformed microstructure, while a saturated aqueous picric acid solution was used to reveal the prior-austenite grain boundaries (PAGBs). Optical microscopy (OM) and scanning electron microscopy (SEM) observations were carried out on Nikon Eclipse LV150 and FEI InspectF, respectively. EBSD mapping was carried out via a FEI Sirion

Field Emission Gun SEM equipped with a HKL Nordlys detector. An orientation map (400 μm×350 μm) with a step size of 0.2 μm and an accelerating voltage of 20 kV was obtained on the RD-ND plane of the continuously cooled specimen.

Oxford Jupiter XR atomic force microscope (AFM) operating in contact mode was used to characterise the surface morphology and measure the height differences between grains. AFM images were obtained in a scan area of 50 μm × 50 μm, with a resolution of 2048× 2048 pixels and a scan rate of 0.4 Hz. The acquired images were subsequently processed using Asylum Research software.

Thin foil samples were prepared using a Helios 5 UC focused ion beam (FIB) for observation via transmission Kikuchi diffraction (TKD). Off-axis TKD was performed at an accelerating voltage of 20 kV with a step size of 0.02 μm. Microstructural characterisation of the thin foils was conducted using a JEOL-2010 transmission electron microscope (TEM) operated at 200 kV. Needle-shaped specimens containing targeted boundaries for atom probe tomography (APT) analysis were cut from bulk material and prepared through the site-specific in-situ lift-out method using FIB. The diameters of the needle tips were controlled to be less than 50 nm. APT was conducted using Cameca LEAP 6000XR in laser pulsing mode at a specimen temperature below 50K. APT data reconstruction and quantitative analysis were performed using AP Suite software.

3 Results

3.1 PAGBs and transformed microstructure

Fig. 1(a)–(b) shows the optical micrographs of PAGBs before and after austenite deformation. Prior to the strain of 0.5 in Fig. 1(a), the austenite grains were fully recrystallized with a mean linear intercept length of 62.8±2.6 μm. After a strain of 0.5 in Fig. 1(b), the austenite microstructure remained in an unrecrystallized state. Fig. 1(c)–(d) presents the OM and SEM micrographs of the transformed microstructure (cooled at 10 °C/s between 950 °C and 500 °C, similarly hereinafter). In Fig. 1(c)–(d), AF can be readily distinguished from BF. Coarse packets of parallel laths were identified as BF, while regions consisting of fine grains with irregular shapes, chaotic and intersecting arrangement were regarded as AF. The inverse pole figure (IPF) coloured orientation map and the boundary map of the transformed microstructure are shown in Fig. 1(e)–(f), respectively. The volume fraction of PF/QF was evaluated using a phase quantification method based on EBSD data [27]. The volume fractions of PF/QF, AF, and BF were quantified as 5.4% ± 0.7%, 31.1% ± 5.0% and 63.5% ± 6.0%, respectively, confirming the dominance of AF and BF. The distribution of boundary misorientation angles in Fig. 1(g) shows low densities between 21° and 47°, providing further evidence that displacive transformation products prevail.

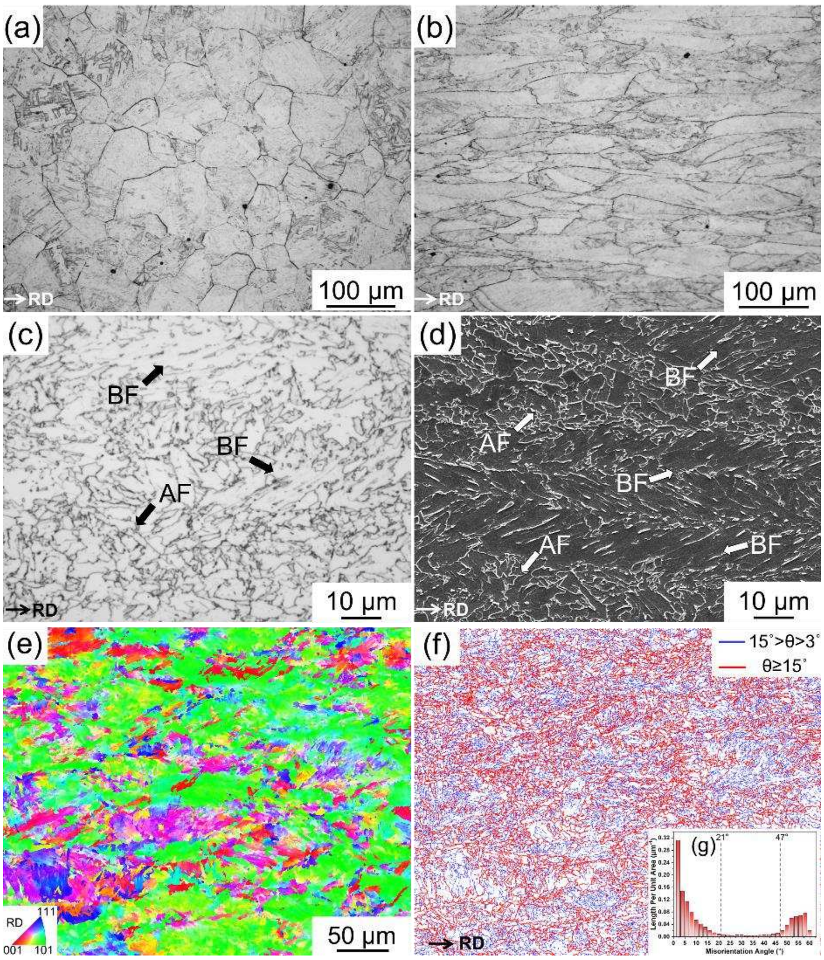

Fig. 1. Optical micrographs depicting prior austenite grain boundaries of specimens water quenched from 950 °C (a) before and (b) after the strain of 0.5. The transformed microstructure (c) optical micrograph, (d) SEM secondary electron micrograph, (e) inverse pole figure coloured orientation map of the transformed microstructure, (f) boundary map where blue lines

represent boundaries with misorientation angles between 3° and 15° and red lines represent boundaries with misorientation angles greater than 15°, and (g) boundary density histograms in terms of length per unit area with misorientation angles from 2° to 63°.

3.2 Reconstruction of deformed austenite orientations

Parent austenite orientation is a prerequisite for analysing the crystallographic characteristics of AF. Reconstruction of parent austenite orientations critically depends on the selection of orientation relationship (OR). In this study, the method proposed in Ref. [28] based on boundary misorientations was used to determine the OR between AF and austenite.

The average OR determined from five AF regions is given in Table 1 together with some ORs obtained in Ref. [18] from bainite transformed isothermally at different temperatures and martensite. ORs are presented as rotations between FCC and BCC in the form of Bunge Euler angles. The angular deviations between close-packed planes ($\Delta\theta_{\mathrm{CP}}$) and close-packed directions ($\Delta\theta_{\mathrm{CD}}$) are also listed in Table 1. It is clear that the average OR calculated from AF regions is very close to the OR of bainite transformed at 580 °C. Although chemical composition and deformation can influence the OR, existing studies indicate that they do not alter the intrinsic dependence of the OR on transformation temperature [18, 28, 29]. The transformation temperature remains the dominant factor governing the evolution of the OR, particularly $\Delta\theta_{\mathrm{CP}}$. Accordingly, the AF in the present study is inferred to have transformed at a relatively high transformation temperature, comparable to approximately 580 °C.

Table 1. OR and misorientation between CP and CD of BCC and FCC. $\Delta\theta_{CP}$ and $\Delta\theta_{CD}$ are the angular deviations between close-packed planes and close-packed directions, respectively.

Microstructure	OR Euler Angles ($\phi1$, Φ, $\phi2$)	$\Delta\theta_{CP}$	$\Delta\theta_{CD}$
Martensite (Ms=440 °C) [18]	(119.9°, 8.8°, 196.0°)	1.5±0.2	2.9±0.1
Bainite (450 °C) [18]	(119.0°, 8.9°, 197.3°)	1.4±0.2	2.6±0.1
Bainite (500 °C) [18]	(117.1°, 8.4°, 199.0°)	1.9±0.4	2.7±0.2
Bainite (580 °C) [18]	(111.9°, 7.7°, 204.3°)	2.9±0.1	2.7±0.1
AF in present study	(114.7°, 7.6°, 201.1°)	2.9±0.3	3.2±0.2

Owing to this OR and the symmetry of austenite, there are 24 variants for each austenite grain. These variants can be grouped into four close-packed plane (CP) groups, each consisting of six variants sharing the same parallel relationship of CPs between AF and austenite. These variants can also be discriminated into three Bain groups according to three distinctive variants of the Bain correspondence. The sequence of the 24 variants and their corresponding CP and Bain groups shown in Ref. [30] were adopted in this research and are shown in Table.S2.

Adopting the determined OR and the austenite orientation reconstruction method proposed in Ref. [24], the orientation map of the deformed austenite was reconstructed and is shown in Fig. 2(a). In this map, black regions represent the locations in which the minimal difference between the experimental data and the variants of the best fitted austenite orientation is higher than 5°, indicating reconstruction failure in these regions. Typically, near the prior-austenite grain boundaries (PAGBs), reconstruction is more likely to fail due to the presence of variants from different austenite grains. Therefore, the black regions in Fig. 2(a) are primarily related to the presence of PAGBs. Since the misorientation angles between variants from the same austenite grain are either less than 21° or larger than 47°, boundaries with misorientation angles between 21°- 47° in the transformed microstructure orientation map (Fig. 2(b)) are used to partly depict PAGBs. A good overall agreement is observed between the black regions in Fig. 2(a) and the partially revealed PAGBs in Fig. 2(b).

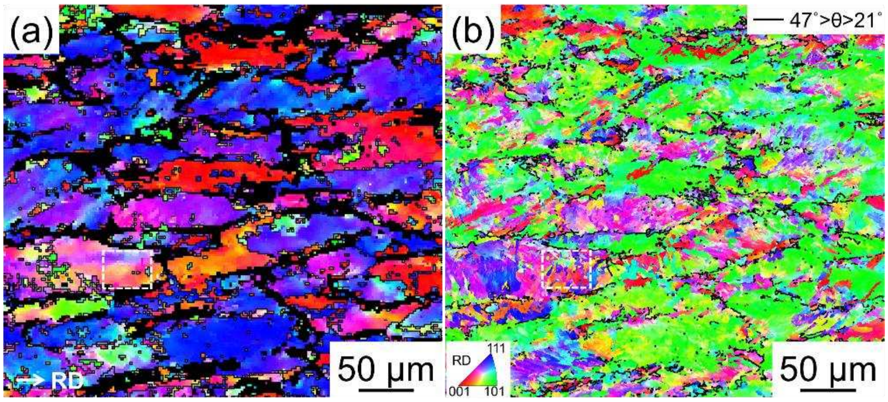

Fig. 2. IPF coloured orientation maps of (a) reconstructed austenite where black lines represent high angle grain boundaries and black regions represent reconstruction failure locations; (b) the transformed microstructure where black lines represent boundaries with misorientation angle between 21°-47°.

3.3 Crystallographic analysis of AF

Detailed crystallographic analysis of AF was conducted in a region transformed from a single deformed austenite grain, as indicated by the area bounded by a dashed rectangle in Fig. 2. Orientations of the deformed austenite in the region are shown in Fig. 3(a). As observed in Fig. 2(a), some inaccurately reconstructed austenite grains appear in the selected region. These were replaced with orientations from neighbouring austenite grains exhibiting the smallest misorientation angles between their variants and the measured BCC orientations. Band contrast map, boundary map and IPF coloured orientation map of the selected region are shown in Fig. 3(b)–(d), respectively. These maps clearly indicate that the transformed microstructure in the selected region consists of fine grains with a chaotic arrangement, irregular grain shapes, and a high density of HAGBs, manifesting a typical AF microstructure.

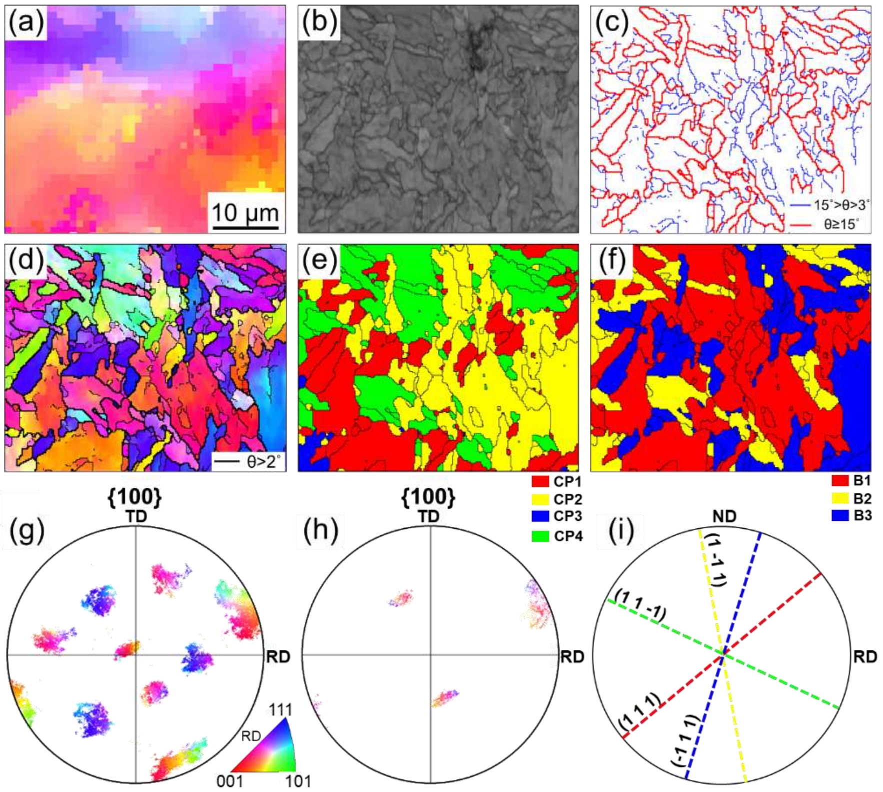

Fig. 3. (a) IPF coloured orientation map of reconstructed austenite in the selected AF region (similarly hereafter), (b) band contrast map, (c) boundary map, (d) IPF coloured orientation map of AF microstructure, (e) CP map, (f) Bain map, (g) {100} pole figure of AF orientations, (h) {100} pole figure of reconstructed austenite orientations and (i) traces of {111}γ planes of the average austenite orientation on the RD-ND plane.

The orientation map can also be modified to display different colours for variants from distinct CP groups or Bain groups, generating the CP map and the Bain map, respectively. This facilitates direct interpretation of variant selection and variant pairing [18]. Fig. 3(e) and f exhibit the CP map and the Bain map of the selected AF region, respectively. The {100} pole figures of the measured AF orientations and the reconstructed austenite orientations are shown in Fig. 3(g) and Fig. 3(h), respectively. The good correspondence between the two demonstrates the correct reconstruction. Fig. 3(i) shows the traces of $\{111\}_\gamma$ planes of the average austenite orientation on the RD-ND plane. The elongated boundary directions of AF laths belonging to the same CP group (Fig. 3(e)) are nearly parallel to the trace directions of the corresponding $\{111\}_\gamma$

planes (Fig. 3(i)). This geometric alignment arises because the elongated boundaries of AF and BF laths on an observation plane coincide with the intersection lines between their habit planes and the observation plane. The six variants belonging to the same CP group share similar habit planes [31], which are all close to the corresponding $\{111\}_\gamma$ planes [1].

In AF/BF dominant microstructures, the impact toughness is closely correlated with the density of HAGB, which is governed by variant pairing behavior, i.e. how variants are arranged relative to each other. Given the 24 possible variants for a single austenite grain, there are 23 possible variant pairs (Table.S2). If all variant pairs are formed equally, the length fraction of each variant pair should be 1/23 (~0.043). To quantify the length fractions of variant pairs, the method given in Ref. [18] which takes into account both the misorientation angles and the axis to identify variant pairs was adopted in this research. A small tolerance angle of 1° was used to avoid the overlap of different variant pairs. Fig. 4(a) shows the length fractions of all variant pairs in the selected AF region. Variant pairs belonging to the same Bain group are indicated by short arrows. Notably, the V1/V4 and V1/V8 pairs within the same Bain group, as well as the V1/V2 pair belonging to the same CP but different Bain groups, are preferentially formed. Fig. 4(b) shows the boundary density distribution as a function of misorientation angle for the selected AF region.

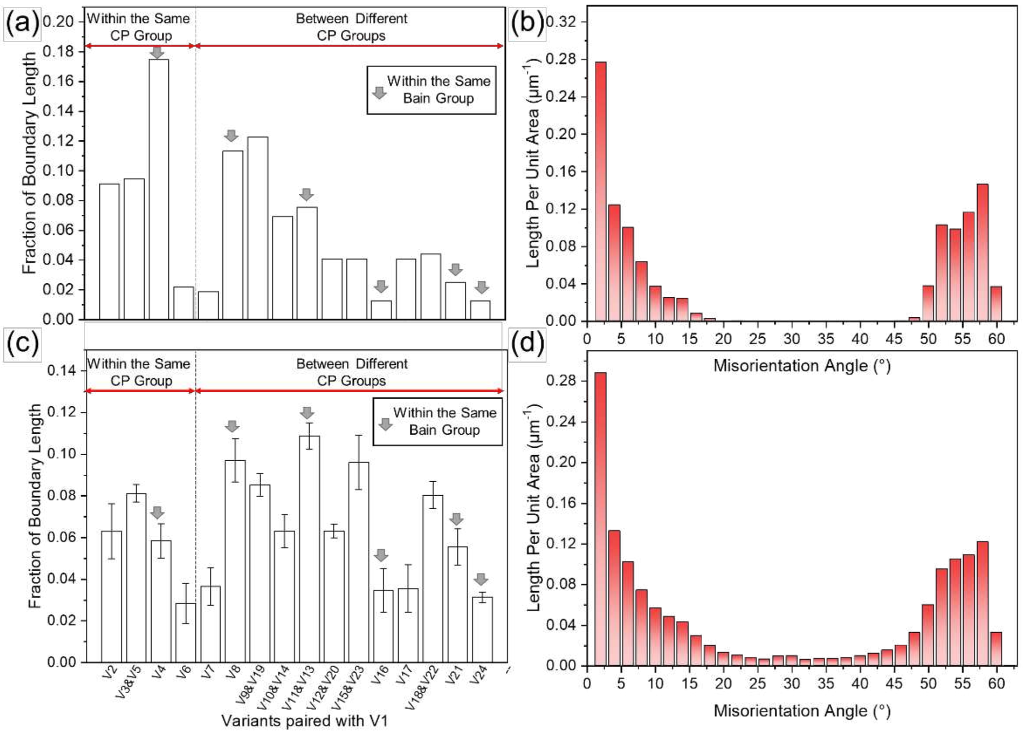

Fig. 4. (a) Length fractions of variant pairs and (b) histograms showing boundary densities in terms of absolute number per unit area with misorientation angles from 2° to 63° for the selected AF region in a single deformed austenite grain; (c) Length fractions of variant pairs and (d) histograms showing boundary densities in terms of absolute number per unit area with misorientation angles from 2° to 63° for the AF identified in the whole EBSD map.

To analyse AF variant pairing on a macroscopic scale, the entire EBSD map was divided into four parts. The length fractions of variant pairs were quantified for the AF microstructure identified in each part. Fractions of each variant pair in the four parts were averaged to give the final results shown in Fig. 4(c). All variant pairs show up and the overall variant pairing is close to a random distribution. Fig. 4(d) shows the boundary density distribution as a function of misorientation angle for the identified AF in the whole EBSD map. The densities of HAGBs in the AF microstructure are larger than those of the whole transformed microstructure in Fig. 1(g).

3.4 Morphological analysis of AF

The same AF microstructure etched with nital was correlatively characterized with OM, SEM, EBSD and AFM, as shown in Fig. 5. After nital etching, the irregular grain shapes, chaotic and intersecting grain arrangement of AF can be revealed in Fig. 5(a)–(b). The mechanisms responsible for the unique morphological features of AF are presented in the Discussion section.

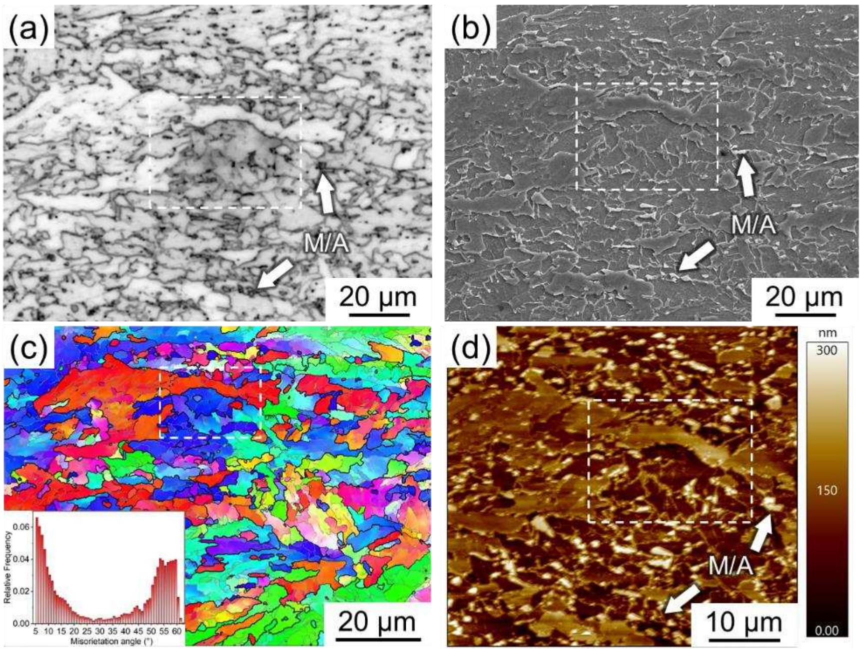

Fig. 5. (a) OM micrograph and (b) SEM secondary electron micrograph and (c) IPF coloured orientation map where black lines represent HAGBs (d) atomic force microscopy micrograph depicting the AF microstructure.

4 Discussion

4.1 Crystallographic characteristics of AF

The crystallographic characteristics of AF can only be appreciated when comparing with other bainitic microstructures reported in the literature [18, 32]. For bainitic microstructures transformed from recrystallized austenite at two different temperatures (450 °C and 580 °C), their crystallographic characteristics were presented in Ref. [18] for a Fe-0.15C-1.5Mn-0.2Si (wt.%) steel and are reproduced in Fig. S4.

At the lower transformation temperature of 450 °C, bainitic laths from the same CP group tend to form side by side (Fig. S4(a)). Conventionally, adjacent laths from the same CP group make up features called packets [30, 33], due to their near parallel lath boundaries. Therefore, the bainitic microstructure formed under this condition has a packet structure. Furthermore, within each packet, laths are generally from various Bain groups in Fig. S4(b), leading to a high density of HAGBs shown as black lines. The above characteristics are also reflected in the results of variant pair fractions shown in Fig. S4(c). Variant pairs belonging to the same CP group are favoured with a total fraction of ~0.76. Among them, the V1/V2 variant pair stands out with a particularly high fraction around 0.46.

At the higher transformation temperature of 580 °C, adjacent laths belong to different CP groups in Fig. S4(d), and they are mostly from the same Bain group in Fig. S4(e). This trend is confirmed by the variant pair fractions presented in Fig. S4(f). Variant pairs such as V1/V8 (0.49), V1/V4 (0.17), V1/V11&V1/V13 (0.12) and V1/V21 (0.06) belonging to the same Bain group are strongly favoured, with their respective fractions indicated in parentheses. Together, the 7 variant pairs from the same Bain group account for 87% of the total boundary length, while all remaining 16 pairs share only 13%, dramatically lower than the random variant pairing condition. Due to the low misorientation angles between variants from the same Bain group (Table.S2), the high length fractions of those variant pairs result in a relatively low density of HAGBs in the microstructure (Fig. S4(e)).

For bainitic microstructures transformed from deformed austenite at temperatures below 430 °C, its crystallographic characteristics were investigated in Ref. [32], and the key findings are reproduced in Fig. S5. As shown in Fig. S5(a)–(c), within each deformed austenite grain, the majority of BF laths belong to a single CP group, suggesting that austenite deformation results in severe variant selection under this condition. Similar results were reported in Ref. [34, 35] as well. Furthermore, as shown in Fig. S5(d), each BF packet contains laths from multiple Bain groups, resulting in a high density of HAGBs shown as black lines in Fig. S5(a).

Although the AF in this research is transformed from deformed austenite and its transformation temperature is relatively high (close to 580 °C proven by its OR), its crystallographic characteristics are not similar to either the BF transformed from deformed austenite case (Fig. S5) or the high transformation temperature BF case in Fig. S4(d)–(f).

Variant selection of AF is greatly weakened. As shown in the CP map (Fig. 3(e)) and the Bain map (Fig. 3(f)) of the selected AF region, variants from multiple CP groups and various Bain groups are present simultaneously within a single deformed prior austenite grain. This behaviour stands in stark contrast to the BF transformed from deformed austenite case, where variant selection is typically confined to nearly a single CP group within each prior austenite grain (Fig. S5(c)). It also differs from BF formed at the high transformation temperature, where the selected variants predominantly belong to the same Bain group (Fig. S4(d)).

Variant pairing of AF is nearly random. While certain variant pairs—such as V1/V8, V1/V2, V1/V4 and V1/V21—exhibit relatively high fractions in AF, the overall variant pairing behaviour remains close to a random distribution, in sharp contrast to that observed in the aforementioned bainitic structures. Specifically, the total fraction of 16 variant pairs from different Bain groups reaches 0.63 in AF (Fig. 4(c)), while this total fraction is only ~0.13 in the high transformation temperature BF case (Fig. S4(f)). Furthermore, for the bainite transformed from deformed austenite (Fig. S5), where each pancaked austenite grain is dominated by variants from nearly a single CP group in Fig. S5(c), variant pairs from the same CP group should be strongly preferred. But in AF, the total length fraction of 18 variant pairs from different CP group reaches 0.77, which is almost identical to the expected random variant pairing level of ~0.78.

In summary, although AF forms through a bainitic transformation mechanism, its crystallographic characteristics differ markedly from those of conventional bainitic microstructures reported in the literature. This distinction is manifested in the selection of variants from multiple CP and Bain groups and the near random variant pairing observed in the AF microstructure.

4.2 Underlying mechanism for AF distinct crystallographic characteristics

The unique crystallographic characteristics of AF can be attributed to the occurrence of multi-variant intragranular nucleation, the arrest of lengthening laths and the self-accommodation of the transformation shape strain during AF transformation. These mechanisms are discussed in the following two sections.

4.2.1 Multi-variant intragranular nucleation and arrest of lengthening laths

The selection of variants from different CP groups in AF can be related to the multi-variant intragranular nucleation on dislocation boundaries and the arrest of lengthening laths at high transformation temperatures in the deformed austenite.

During austenite deformation, duplex or more complicated slip systems are activated within each grain, giving rise to intersecting dislocation boundaries on different planes [36, 37]. Based on the relationship between lattice rotations and shear amplitudes of different slip systems [38], it can be inferred that the operation of slip systems with different shear amplitudes leads to the formation of dislocation boundaries with different misorientation angles. Dislocation boundaries with different planes and misorientation angles in the deformed austenite are schematically illustrated in Fig. 6(a), thicker lines representing boundaries with higher misorientation angles. For convenience, dislocation boundaries with the highest misorientation angles in the whole austenite grain are called overall primary dislocation boundaries (OPDBs), while those with the highest misorientation angles in a small local area are called local primary dislocation boundaries (LPDBs).

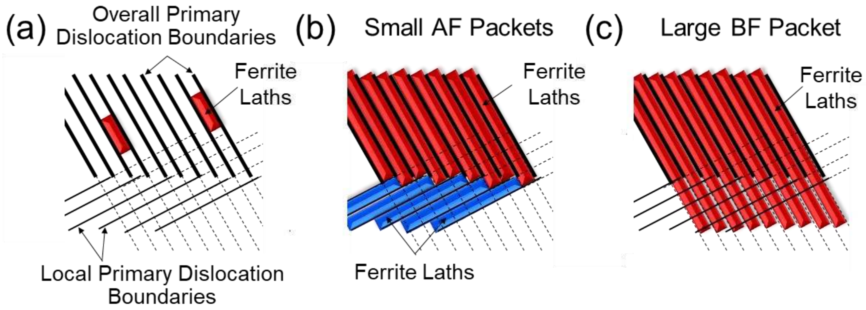

Fig. 6. Schematic illustrations in a heavily deformed austenite region of (a) inhomogeneous austenite deformation substructures, (b) small and intersecting AF packets formed at relatively high temperatures and (c) large BF packets formed at relatively low temperatures.

Dislocation boundaries have an impact on the variant selection of displacive transformation products. For martensite nucleation at these boundaries, it has been demonstrated that the activation energy can be reduced to as little as 0.3% – 24% of that required for normal nucleation [24]. Furthermore, nucleation preferentially occurs for variants whose habit planes are nearly parallel to the dislocation boundaries. Variant selection induced by dislocation boundaries has been confirmed by experimental observations both in martensite and bainite [16, 35, 39].

The selection of variants from multiple CP groups in the AF region (Fig. 3(e)) can be understood by considering both the dislocation-boundary-assisted nucleation mechanism introduced above and the conditions for AF formation proposed in Ref. [23]. As the nucleation activation energy is inversely related to the dislocation boundary energy [24], the potency of a dislocation boundary as nucleation sites depends on its boundary energy, and thus its misorientation angle. The higher the misorientation angle, the more potent the boundary is. Therefore, during transformation, laths from the CP group with habit planes parallel to OPDBs will first nucleate on these boundaries, as schematically illustrated in Fig. 6(a).

However, dislocation boundaries not only act as nucleation sites but also as obstacles impeding the lengthening of bainitic laths, through a mechanism known as mechanical stabilization [40, 41]. At relatively high transformation temperatures, the transformation driving force is inadequate for these initially nucleated laths to overcome LPDBs intersecting with OPDBs, resulting in the arrest of lengthening laths at LPDBs. This arrest creates an opportunity for laths from other CP groups to nucleate on less potent LPDBs, with their habit planes parallel to LPDBs as illustrated in Fig. 6(b). Due to the heterogeneity of deformed austenite substructures [36], this phenomenon can occur at different locations within a deformed austenite grain. Therefore, the multi-variant intragranular nucleation on dislocation boundaries and the arrest of lath lengthening at high transformation temperatures result in the selection of variants from different CP groups and thus the variant pairs belonging to different CP groups.

In contrast, at lower transformation temperatures, the increased transformation driving force reduces the ability of LPDBs to arrest lath lengthening. Under these conditions, laths from the CP group with habit planes parallel to OPDBs can grow across the entire austenite grain. In this case, variants from a single CP group are selected as shown schematically in Fig. 6(c), leading to severe variant selection and the same CP group variant pairing. Such behaviour is exemplified in Fig. S5(c) where the transformation temperature is below 430 °C [32].

4.2.2 Self-accommodation of transformation shape strain

In the selected AF region, it is evident that some adjacent variants belonging to the same CP group are from different Bain groups (Fig. 3(f)). This phenomenon is also reflected in AF variant pairing, V1/(V2-V6) variant pairs appearing both in the selected AF region in Fig. 4(a) and in the entire AF microstructure in Fig. 4(c).

The presence of variant pairs from the same CP group but different Bain groups in AF can be attributed to the self-accommodation of the transformation shape strain. During bainitic transformation, the shape strain is a combination of a large shear strain (≈ 0.26) on the habit plane and a smaller dilatational strain (≈ 0.03) normal to the habit plane [1]. This shape strain can be accommodated through various mechanisms, such as plastic deformation of austenite and bainite, elastic deformation of both phases, and self-accommodation [42]. As discussed in Ref. [30], the formation of variant pairs from the same CP group but different Bain groups effectively accommodates the transformation shape strain. Such self-accommodation occurs when elastic strain accommodation is limited and plastic deformation of austenite becomes difficult [43]. For instance, previous research [18] demonstrated that lowering the transformation temperature to 450 °C increases the strength of austenite, thereby promoting self-accommodation. Using an empirical equation for austenite strength [44], the strength of austenite at 450 °C was estimated as 63.0 MPa for the steel investigated in Ref. [18]. Under this austenite strength condition, variant pairs belonging to the same CP group but from different Bain groups are favoured in Fig. S4(c).

In this research, the transformation temperature of AF is relatively high (around 580 °C), and the austenite strength at 580 °C is estimated as 40.2 MPa for the tested steel, significantly lower than that in the above self-accommodation case (63.0 MPa). However, austenite was deformed before transformation in this research, and work-hardening contributes to the strengthening of austenite. Based on the model proposed in Ref. [41], the strength increase due to work-hardening can be expressed as:

$$M\frac{Gb}{8\pi(1-\upsilon)}\sqrt{\frac{\varepsilon(\delta+D\varepsilon)}{\delta bD}} \tag{1}$$

where M is the Taylor factor for FCC metal, G the shear modulus, v the Poisson's ratio, b the Burgers vector, ε the strain volume, D the austenite grain size before deformation and δ a coefficient equal to ~1 μm [41]. Based on the tested steel chemical compositions, G ,v and b at 580 °C were calculated as 5.54×10^{10} Pa, 0.327 and 2.56×10^{-10} m [45], respectively. After a strain of 0.5, the strength increased by work-hardening was calculated as 81.5 MPa with M of 3.06 [46], D of 62.8 μm. Considering this work-hardening, the strength of the deformed austenite at 580 °C for the tested steel is estimated as 121.7 MPa, substantially higher than that in the above self-accommodation case. Therefore, self-accommodation of transformation strain is expected to occur even at 580 °C or higher in the deformed austenite of the tested steel, promoting the formation of variants and variant pairs from the same CP group but belonging to different Bain groups in AF.

4.3 Origin of AF unique morphology

Metallographic identification of AF morphology relies on developing a sharply delineated and contrasty enough surface, typically achieved by nital etching. In the first place, it is necessary to understand how the morphology of AF becomes observable. Combining the results in Fig. 5, it was found that AF morphology can be observed under three distinct situations.

The first situation involves metallographic contrast generated by crystal faceting, which creates topographical steps at grain boundaries. As shown in Fig. 7, the surface height varies from grain1 to grain2, reflecting differences in chemical reactivity between grains during nital etching. Bonyar et al. [47, 48] proved that the slowest etching rate occurs on a {100} crystal surfaces, while the etching rate of a {111} surface is approximately twice as fast as that of the {100} surface. This is consistent with our observations in Fig. 7(b)–(c), where grain 1 with its {100} plane parallel to the observation plane, appears higher than grain 2 with its {111} plane parallel to the plane.

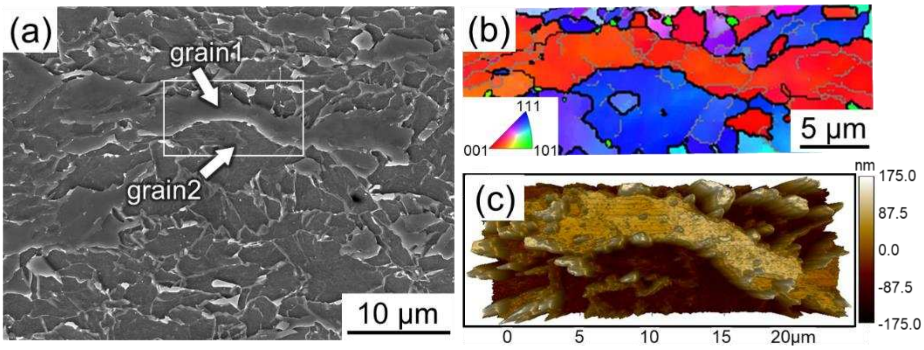

Fig. 7. (a) SEM secondary electron micrograph and (b) IPF coloured orientation maps where black lines represent HAGBs (c) AFM micrograph depicting the AF microstructure in the same region.

The second situation involves metallographic contrast arises from the presence of

M/A constituents. As revealed in Fig. 5, the highest areas in the AFM image correspond to M/A constituents, which appear as the bright regions in the SEM image but the dark ones in the OM image. Boundaries between laths can be revealed when M/A constituents are present, as confirmed by the correlative OM, SEM, and AFM characterization results shown in Fig. 8 for a region selected from Fig. 5 shown by dashed rectangles. In Fig. 8(c)–(e), some lath boundaries are revealed due to the elevated M/A constituents. Angeli et al. [49] proposed that phases with higher carbon contents exhibit higher resistance to nital etching and thus elevated surface. The higher surface height of M/A after etching is attributed to their high carbon contents [50].

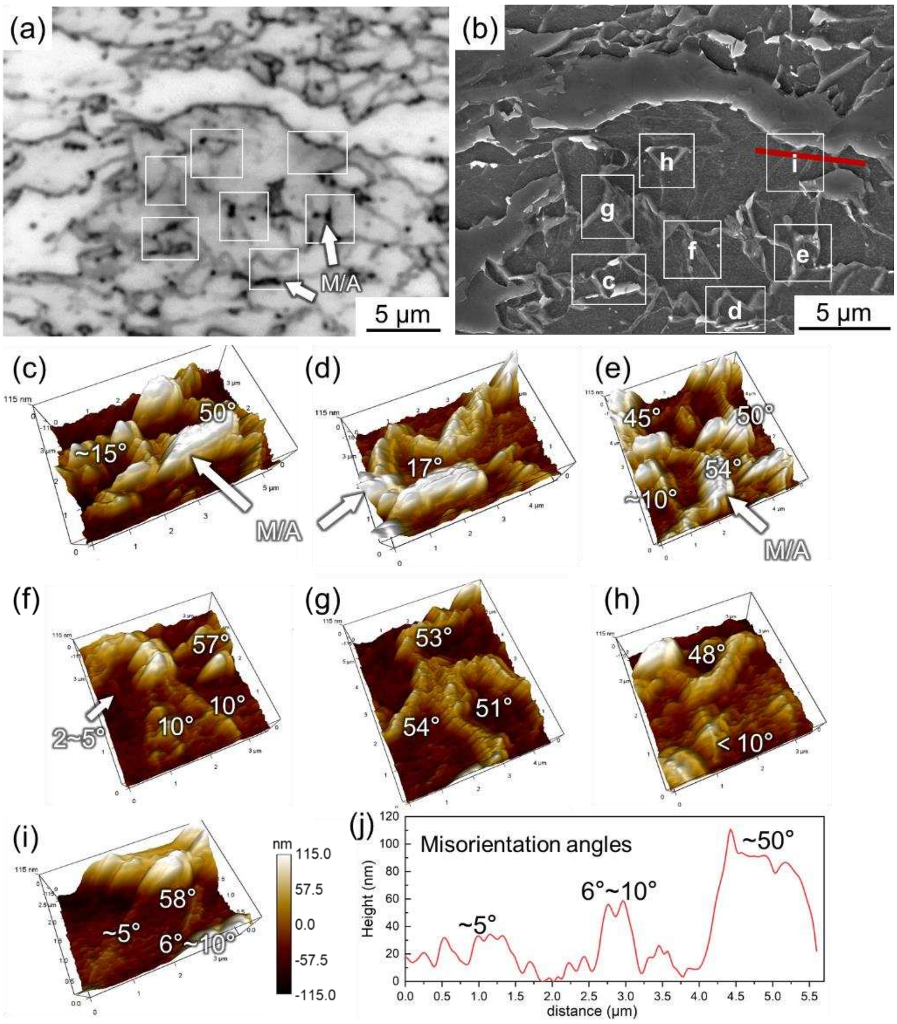

Fig. 8. (a) OM micrograph and (b) SEM secondary electron micrograph of an AF microstructure; (c-i) enlarged AFM images of local grain boundaries; (j) the height difference from the AFM line scan results crossing different grain boundaries of (i).

The third situation involves the surface protrusions associated with HAGBs ($\theta \geq 15°$), which appear dark in OM and bright in SEM. As shown in Fig. 8(f)–(i), the areas surrounding HAGBs exhibit greater surface height compared to those near LAGBs ($\theta < 15°$). This height difference is further confirmed by an AFM line scan across different grain boundaries indicated in Fig. 8(b) by a red line, and the results are shown in Fig. 8(j). This height difference leads to contrasty features around HAGBs while relatively vague features around LAGBs. The vague features around LAGBs can be observed under high-magnification SEM but is barely observable under OM.

Contrary to the conventional understanding presented in materials science textbooks that grain boundaries tend to form grooves after nital etching [51], AFM results reveal that boundaries often exhibit protrusions. To investigate whether these protrusions are related to the existence of thin M/A constituents between grain boundaries, the area in Fig. 8(h) was selected and further characterized. With FIB, the area in Fig. 8(h) was identified in Fig. 9(a). A TEM sample at this location was prepared using FIB and observed under TKD and TEM. The results of TKD in Fig. 9(b) and TEM in Fig. 9(c)–(d) both indicate that the grain boundary protruding morphology is not related to M/A constituents.

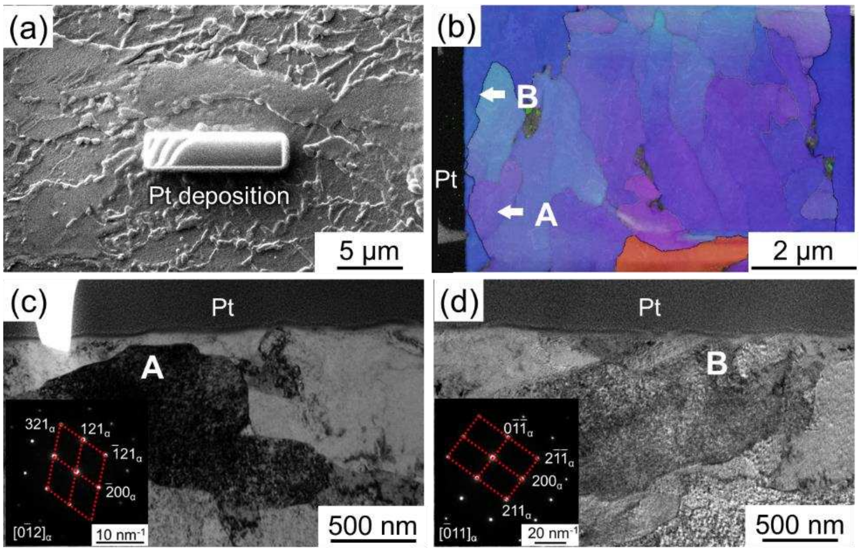

Fig. 9. (a)SEM image of Pt deposition layer (b) Transmission Kikuchi diffraction of the specimen (c,d) high magnified TEM image and electron-beam diffraction (SAED) patterns of corresponding selected area A and B.

To investigate the formation mechanism of surface protrusions associated with grain boundaries, APT analyses were conducted on two grain boundaries—GB1 and GB2—focusing on the chemical composition near the boundaries. Field desorption images of the grains above and below GB1 were processed using the AP Suite software and are shown in Fig. 10(a). Crystallographic poles and zone lines were clearly identified in Fig. 10(a). Orientation imaging microscopy analysis revealed that the misorientation angle between the adjacent grains was only 5.3°. Similarly, based on the poles observed in the desorption map in Fig. 10(d), the misorientation angle of GB2 was determined to be 12.6°. According to the APT reconstruction results shown in Fig. 10(b), carbon segregation was observed at GB1. Compared to the matrix carbon concentration of 0.2 at.%, the carbon concentration at this boundary increases to 0.57 at.%. In Fig. 10(e)–(f), more pronounced carbon segregation was observed at the GB2, where the carbon concentration reached 1.07 at.%. Similarly, Felfer et al. [52] had confirmed that carbon segregates at the boundaries between BF laths using APT, and carbon segregation content at boundaries is correlated with the boundary misorientation angle. Herbig et al. [53] also reported that carbon segregation at random ferrite grain boundaries increased with increasing misorientation up to 14° and became constant with further increase of the misorientation. Carbon plays a critical role in the electric potential difference, with carbon-rich areas exhibiting higher electric potentials and greater resistance to nital etching [54]. Therefore, the protruding morphology of grain boundaries in this research is linked to carbon segregation.

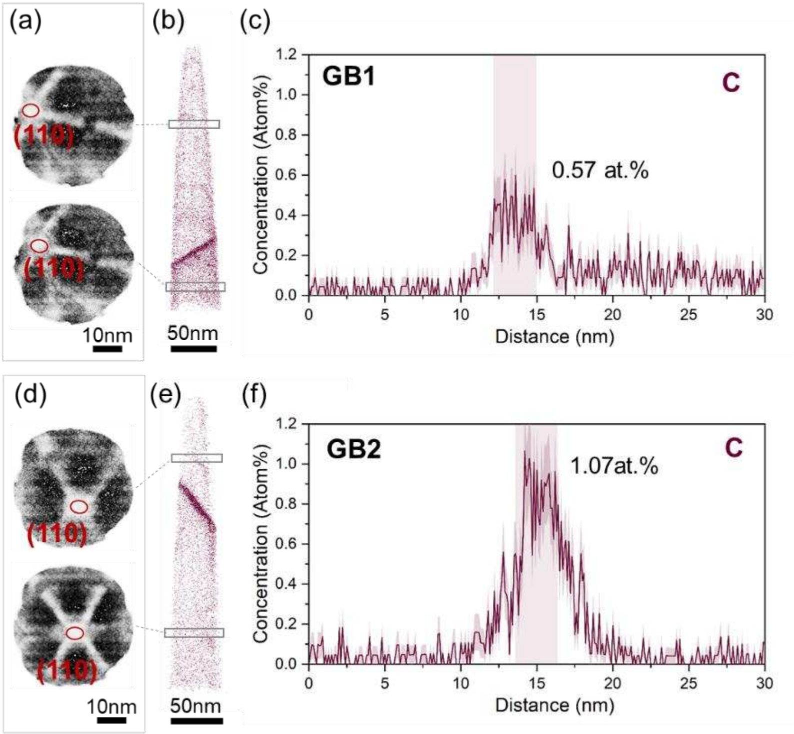

Fig. 10. Field desorption image of grains above and below GB1 (a) and GB2 (d), reconstructed three-dimensional atom maps, revealing C segregation to GB1 (b) and GB2 (e); composition profiles of carbon near GB1 (c) and GB2 (f) measured using cylinders of the same volume with the z-axis parallel to each grain boundary plane normal.

The unique morphological features of AF can be attributed to AF's distinct crystallographic characteristics and the above boundary revelation mechanisms. Firstly, a significant proportion of lath boundaries in AF can be revealed after nital etching. This is because the selection of variants from multiple Bain groups and the near-random variant pairing of AF result in a significant proportion of AF lath boundaries being HAGBs, as proved in Fig. 4(d). These boundaries can be revealed through surface protrusion or crystal faceting after nital etching. Furthermore, since AF forms at relatively high transformation temperatures, carbon partitioning between laths and retained austenite is pronounced, promoting the formation of M/A constituents. These M/A constituents located between laths further contribute to the delineation of lath boundaries. Secondly, the selection of variants from multiple CP groups in AF leads to lath boundaries oriented in various directions within the observation plane. When revealed through etching, these multidirectional boundaries create the chaotic and intersecting appearance of the AF microstructure. Finally, as a result of the variant selection from multiple CP groups and the near-random variant pairing in AF, a "grain" bounded by etching-revealed boundaries may consist of either a single lath or several laths belonging to the same or different CP groups. This gives rise to the irregular grain shapes observed for AF. This point can be roughly understood from Fig. 3(c), where regions bounded only by HAGBs already show irregular shapes.

Based on the above analysis, achieving an AF microstructure with higher strength and toughness requires further refinement of AF grains. This can be realized by increasing the number of AF nucleation sites and controlling the phase transformation to occur within a relatively high-temperature range. Specifically, increasing the degree of austenite deformation, reducing the prior austenite grain size, increasing the strain rate, and initiating cooling immediately after deformation can all enhance the dislocation substructure density in austenite, thereby promoting AF nucleation. In addition, by designing an appropriate cooling schedule, it is possible to suppress the formation of polygonal ferrite, which reduces strength, while ensuring that the transformation mainly occurs within a temperature range where the dislocation substructure effectively impedes lath growth. This helps to prevent excessive lath lengthening and suppresses the transition from AF to BF. As a result, both the volume fraction of AF and the refinement of AF grains can be improved.

The findings of this research clarify the crystallographic characteristics of acicular ferrite, and elucidate the mechanisms responsible for its crystallographic and morphological features. These insights advance the understanding and characterization of AF and provide a basis for weakening variant selection and forming random variant pairing by austenite deformation and appropriate cooling.

5 Conclusions

In this research, a HSLA steel was subjected to plane strain compression and continuous cooling to investigate the crystallographic and morphological characteristics of acicular ferrite (AF). The following conclusions were drawn:

(1) The orientations relationship between AF and austenite is close to that of bainite transformed at 580 °C in the literature, indicating that the transformation temperature of AF is relatively high.

(2) Crystallographic characteristics of AF are manifested in the selection of variants from multiple close-packed plane (CP) and Bain groups and the near random variant pairing. This is distinct from those observed in other bainitic microstructures in the literature exhibiting variants selected from either the same CP or the same Bain group and preferential variant pairing.

(3) AF unique crystallographic characteristics can be attributed to the occurrence of multi-variant intragranular nucleation, arrest of lengthening laths and self-accommodation of the transformation shape strain during AF transformation, all driven by austenite deformation and proper cooling.

(4) Boundaries between AF laths can be observed after nital etching under three distinct situations, including crystal faceting, martensite/austenite (M/A) constituent delineating and surface protrusions induced by carbon segregation at grain boundaries. Boundaries with larger misorientation angles are associated with higher carbon segregation levels, resulting in more pronounced surface protrusions and improved visibility of the boundary.

(5) Distinct AF morphology including chaotic and intersecting arrangement and irregular grain shapes is attributed to AF’s distinct crystallographic characteristics and the above boundary revelation mechanisms.

Acknowledgements

This work was financially supported by the National Natural Science Foundation of China (No.U24A20105, No.52293390, No.52293393), the Major Scientific and Technological Innovation Project of CITIC Group (Grant Number 2022zxkya06100), Liaoning Academy of Materials and Companhia Brasileira de Metalurgia e Mineração (CBMM).

References

[1] H.K.D.H. Bhadeshia, Bainite in steels,Third ed., Institute of Materials, London, 1992. pp.251-254.

[2] Y. Smith, A. Coldren, R. Cryderman, Toward improved ductility and toughness, Climax Molybdenum Company (Japan) Ltd, Kyoto, 1972, pp. 119-142.

[3] Y. Shao, C. Liu, Z. Yan, H. Li, Y. Liu, J. Mater. Sci. Technol. 34(5) (2018) 737-744.

[4] M. Pontremoli, P. Bufalini, A. Aprile, C. Jannone, Metals Tech. 11(1) (1984) 504-514.

[5] R.L. Cryderman, A.P. Coldren, J.R. Bell, J.D. Grozier, ASM Trans. Quart. 62(3) (1969) 561-574.

[6] H. Zhao, E. Palmiere, Metall. Mater. Trans. A 48(7) (2017) 3389-3399.

[7] Y.M. Kim, S.Y. Shin, H. Lee, B. Hwang, S. Lee, N.J. Kim, Metall. Mater. Trans. A 38(8) (2007) 1731-1742.

[8] X. Wu, H. Lee, Y.M. Kim, N.J. Kim, J. Mater. Sci. Technol. 28(10) (2012) 889-894.

[9] T. Chiba, G. Miyamoto, T. Furuhara, Scr. Mater. 67(4) (2012) 324-327.

[10] P.P. Suikkanen, C. Cayron, A.J. DeArdo, L.P. Karjalainen, J. Mater. Sci. Technol. 27(10) (2011) 920-930.

[11] P.P. Suikkanen, C. Cayron, A.J. DeArdo, L.P. Karjalainen, J. Mater. Sci. Technol. 29(4) (2013) 359-366.

[12] A. Shibata, G. Miyamoto, S. Morito, A. Nakamura, T. Moronaga, H. Kitano, I. Gutierrez-Urrutia, T. Hara, K. Tsuzaki, Acta Mater. 246 (2023) 118675.

[13] H. Feng, H. Wang, H. Li, H. Zhu, S. Zhang, Z. Jiang, J. Mater. Sci. Technol. 215(2025) 244-257.

[14] H. Sun, Y. Wang, Z. Wang, N. Liu, Y. Peng, X. Zhao, R. Ren, H. Zhang, J. Mater. Sci. Technol. 49 (2020) 126-132.

[15] T. Furuhara, H. Kawata, S. Morito, G. Miyamoto, T. Maki, Metall. Mater. Trans. A 39(5) (2008) 1003-1013.

[16] G. Miyamoto, N. Iwata, N. Takayama, T. Furuhara, Acta Mater. 60(3) (2012) 1139-1148.

[17] J. Wang, M. Huang, J. Hu, C. Wang, W. Xu, J. Mater. Sci. Technol. 69 (2021) 148-155.

[18] N. Takayama, G. Miyamoto, T. Furuhara, Acta Mater. 60(5) (2012) 2387-2396.

[19] X. Zhang, C. Chen, Q. Li, T. Zhao, D. Sun, S. Liu, Z. Yang, B. Lv, F. Zhang, J. Mater. Sci. Technol. 258 (2026) 228-241.

[20] S. Yamamoto, H. Yokoyama, K. Yamada, M. Niikura, ISIJ Int. 35(8) (1995) 1020-1026.

[21] C. Chiou, J. Yang, C. Huang, Mater. Chem. Phys. 69(1) (2001) 113-124.

[22] Y.M. Kim, H. Lee, N.J. Kim, Mater. Sci. Eng. A 478(1) (2008) 361-370.

[23] H. Zhao, B.P. Wynne, E.J. Palmiere, J. Mater. Sci. 53(5) (2018) 3785–3804.

[24] G. Miyamoto, N. Iwata, N. Takayama, T. Furuhara, Acta Mater. 58(19) (2010) 6393-6403.

[25] J.S. Hinton, Laboratory simulation of microstructural evolution in AISI 430 Ferritic Stainless Steel during the Steckel Mill Process, Ph.D Thesis, University of Sheffield, 2006.

[26] L. Sun, The effects of strain path reversal on austenite grain subdivision, recrystallisation and phase transformations in microalloyed steel,Ph.D Thesis, University of Sheffield, 2012.

[27] H. Zhao, B. Wynne, E. Palmiere, Mater. Charact. 123 (2017) 339-348.

[28] N. Zolotorevsky, S. Panpurin, A. Zisman, S. Petrov, Mater. Charact. 107 (2015) 278-282.

[29] A. Ståhlkrantz, P. Hedström, N. Sarius, A. Borgenstam, Metall. Mater. Trans. A 53(9) (2022) 3418-3427.

[30] S. Morito, H. Tanaka, R. Konishi, T. Furuhara, T. Maki, Acta Mater. 51(6) (2003) 1789-1799.

[31] T. Furuhara, N. Takayama, G. Miyamoto, Mater. Sci. Forum 638 (2010) 3044-3049.

[32] N. Bernier, L. Bracke, L. Malet, S. Godet, Metall. Mater. Trans. A 45(13) (2014) 5937-5955.

[33] T. Furuhara, H. Kawata, S. Morito, T. Maki, Mater. Sci. Eng. A 431(1) (2006) 228-236.

[34] N.Y. Zolotarevskii, A.A. Zisman, S.N. Panpurin, Y.F. Titovets, S.A. Golosienko, E.I. Khlusova, Met. Sci. Heat Treat 55(9) (2014) 550-558.

[35] L. Malet, M. Barnett, P. Jacques, S. Godet, Scr. Mater. 61(5) (2009) 520-523.

[36] A.S. Taylor, P. Cizek, P.D. Hodgson, Acta Mater. 60(4) (2012) 1548-1569.

[37] G. Winther, X. Huang, Philos. Mag. 87(33) (2007) 5215-5235.

[38] G. Winther, Acta Mater. 56(9) (2008) 1919-1932.

[39] G. Miyamoto, N. Iwata, N. Takayama, T. Furuhara, J. Alloy Compd. 577 (2013) S528-S532.

[40] P. Shipway, H. Bhadeshia, Mater. Sci. Tech. 11(11) (1995) 1116-1128.

[41] S. Chatterjee, H.-S. Wang, J. Yang, H. Bhadeshia, Mater. Sci Tech. 22(6) (2006) 641-644.

[42] S. Zhang, S. Morito, Y.-i. Komizo, ISIJ Int. 52(3) (2012) 510-515.

[43] A. Lambert-Perlade, A.-F. Gourgues, A. Pineau, Acta Mater. 52(8) (2004) 2337-2348.

[44] S.B. Singh, H.K.D.H. Bhadeshia, Mater. Sci. Eng. A 245(1) (1998) 72-79.

[45] S. Van Bohemen, Scr. Mater. 75 (2014) 22-25.

[46] R. Stoller, S. Zinkle, J. Nucl. Mater. 283 (2000) 349-352.

[47] A. Bonyár, J. Renkó, D. Kovács, P.J. Szabó, Mater. Charact. 156 (2019) 109844.

[48] P.J. Szabó, A. Bonyár, Micron 43(2) (2012) 349-351.

[49] J. Angeli, E. Füreder, M. Panholzer, A.C. Kneissl, Pract. Metallogr. 43(10) (2006) 489-504.

[50] N. Takayama, G. Miyamoto, T. Furuhara, Acta Mater. 145 (2018) 154-164.

[51] D.G. Rethwisch, J. Callister William D., Mater. Sci. Eng. An Introduction, 10th Edition ed., Hoboken, NJ : Wiley, the United States of America, 2018.

[52] P.J. Felfer, C.R. Killmore, J.G. Williams, K.R. Carpenter, S.P. Ringer, J.M. Cairney, Acta Mater. 60(13-14) (2012) 5049-5055.

[53] M. Herbig, D. Raabe, Y.J. Li, P. Choi, S. Zaefferer, S. Goto, Phys. Rev. Lett. 112(12) (2014) 126103.

[54] S. Reisinger, G. Ressel, S. Eck, S. Marsoner, Micron 99 (2017) 67-73.